Manipulation of magnetic dipole emission from Eu^{3+} with Mie-resonant dielectric metasurfaces

Aleksandr Vaskin,[*,†] Soheila Mashhadi,[‡] Michael Steinert,[†] Katie E. Chong,[¶] David Keene,[§] Stefan Nanz,[‖] Aimi Abass,[⊥] Evgenia Rusak,[‖,¶] Duk-Yong Choi,[#] Ivan Fernandez-Corbaton,[⊥] Thomas Pertsch,[†] Carsten Rockstuhl,[⊥,‖] Mikhail A. Noginov,[‡] Yuri S. Kivshar,[¶] Dragomir N. Neshev,[¶] Natalia Noginova,[‡] and Isabelle Staude[†]

†*Institute of Applied Physics, Abbe Center of Photonics, Friedrich Schiller University Jena, 07745 Jena, Germany*

‡*Center for Materials Research, Norfolk State University, Norfolk, VA 23504*

¶*Nonlinear Physics Centre, Australian National University, Canberra ACT 2601, Australia*

§*Center for Materials Research, Norfolk State University, Norfolk, VA 23504*

‖*Institute of Theoretical Solid State Physics, Karlsruhe Institute of Technology, 76131 Karlsruhe, Germany*

⊥*Institute of Nanotechnology, Karlsruhe Institute of Technology, 76021 Karlsruhe, Germany*

#*Laser Physics Centre, Research School of Physics and Engineering, The Australian National University, Canberra, ACT 2601, Australia*

E-mail: aleksandr.vaskin@uni-jena.de

Abstract

Mie-resonant high-index dielectric nanoparticles and metasurfaces have been suggested as a viable platform for enhancing both electric and magnetic dipole transitions of fluorescent emitters. While the enhancement of the electric dipole transitions by such dielectric nanoparticles has been demonstrated experimentally, the case of magnetic-dipole transitions remains largely unexplored. Here, we study the enhancement of spontaneous emission of Eu^{3+} ions, featuring both electric and magnetic-dominated dipole transitions, by dielectric metasurfaces composed of Mie-resonant silicon nanocylinders. By coating the metasurfaces with a layer of an Eu^{3+} doped polymer, we observe an enhancement of the Eu^{3+} emission associated with the electric (at 610 nm) and magnetic-dominated (at 590 nm) dipole transitions. The enhancement factor depends systematically on the spectral proximity of the atomic transitions to the Mie resonances as well as their multipolar order, which is controlled by the nanocylinder radius. Importantly, the branching ratio of emission via the electric or magnetic transition channel can be modified by carefully designing the metasurface, where the magnetic dipole transition is enhanced more than the electric transition for cylinders with radii of about 130 nm. We confirm our observations by numerical simulations based on the reciprocity principle. Our results open new opportunities for bright nanoscale light sources based on magnetic transitions.

In optics, the interaction of matter with the magnetic field of light is usually ignored since it is several orders of magnitude weaker as compared to the interaction of matter with the electric field of light. An important exception, however, is exemplified by trivalent lanthanide ions, such as Eu^{3+} and Er^{3+}, which are well known to exhibit magnetic-dipole transitions in the visible and near-infrared region, respectively. Trivalent lanthanides have been intensely studied for a few decades and remain an active subject of research. [1–3] Recently, for example, Novotny *et al.* [2] demonstrated that the magnetic dipole transition of Eu^{3+} ions can be selectively excited using azimuthally polarized focused laser beams possessing high magnetic and vanishing electric field at the centre. As such, the engineering of the optical

excitation has proven to be an effective way to influence how lanthanide ions interact with light.

Another important factor governing the light-matter interaction of lanthanide ions is their photonic environment. It has a crucial influence on the spontaneous emission *via* both electric and magnetic dipole transitions. This influence was first described by Purcell for magnetic dipole radiation[4] and later generalized for both electric and magnetic emission through the so-called Purcell factor (see Baranov, *et al.*[5] for a recent review). Thus, proper engineering of the photonic environment as such could dramatically influence the selectivity between the electric and magnetic emission channels. In that respect, optical metamaterials and metasurfaces offer unique opportunities for design of the electric and magnetic near-field environment and hence for selectively enhancing the emission rates of electric or magnetic emitters.

Indeed, the modification of the local density of optical states (LDOS) and the manipulation of magnetic dipole spontaneous emission have been studied using various photonic structures,[6–13] including metallic mirrors, metal films, hyperbolic metamaterials, and plasmonic micro- and nanostructures. Resonant plasmonic metasurfaces consisting of an array of nanoholes in a bilayer gold film[11] have shown a clear difference in the enhancement of the magnetic dipole transition with respect to the electric transition. Designed to support plasmonic resonances overlapping with the emission spectrum of the Eu^{3+} ions, the nanohole metasurface allowed for preferential enhancement only of the magnetic emission.

However, in the vicinity to plasmonic nanostructures the intrinsic absorption losses of metals at optical frequencies can result in quenching of the emission. To overcome this limitation, high-index dielectric nanoparticles and metasurfaces[14–19] have been suggested as an alternative platform to efficiently tailor the magnetic LDOS and selectively enhance magnetic radiative decay.[20,21] For a sufficiently high index contrast to the environment, dielectric nanoparticles can support both electric and magnetic multipolar Mie-type resonances in the visible, which can be tailored by the nanoparticle geometry.[14,15] In particular, it was shown

theoretically that near-infrared quadrupolar magnetic resonances in silicon particles can preferentially promote magnetic versus electric radiative de-excitation in trivalent erbium ions at 1.54 μm.[20]

The enhancement of the magnetic dipole emission was also studied, both analytically and numerically, for a variety of dielectric nanoparticles, including nanospheres[22] and hollow nanodisks.[23,24] In the latter case, it was predicted that the emission can be significantly enhanced near the magnetic dipole resonance, while electric dipole emission will be suppressed when emitters are located in a hollow of the nanodisk.[23] A recent experimental work mapped the spatial distributions of the relative magnetic and electric radiative LDOS and showed magnetic emission enhancement near photonic nanoantennas featuring magnetic dipolar or electric monopolar resonances, which were carved by a focused-ion beam (FIB) at the extremity of a near-field tip.[25] However, experimental demonstrations of the magnetic-dipole emission enhancement and manipulation by integrated nanostructures composed of Mie-resonant dielectric nanoparticles are still missing.

In this work, we probe experimentally the modification of magnetic and electric LDOS in an integrated resonant nanophotonic architecture consisting of Mie-resonant dielectric metasurfaces. The metasurfaces are composed of silicon nanocylinders arranged in a square array and covered by a thin layer of a Eu^{3+} containing polymer, as conceptually illustrated in Fig. 1. We fabricate different metasurfaces featuring a systematic variation of the nanocylinder radius, which allows us to vary the spectral position of their electric and magnetic quadrupolar dominated Mie-type resonances over a broad spectral range. We map selectively the emission of the Eu^{3+} ions at the electric and magnetic transition at 610 nm and 590 nm, respectively. For quantitative analysis, we determine the ratio of the emission enhancements via the two distinct channels as a function of the nanocylinder radius. As a central result of this work, we demonstrate experimentally, for the first time, that a Mie-resonant all-dielectric metasurface allows for selective enhancement of the magnetic dipole emission over the electric dipole emission for a proper choice of the metasurface geometry. We confirm our experimen-

tal observations with numerical simulations taking the periodic boundary conditions of the metasurface into account.

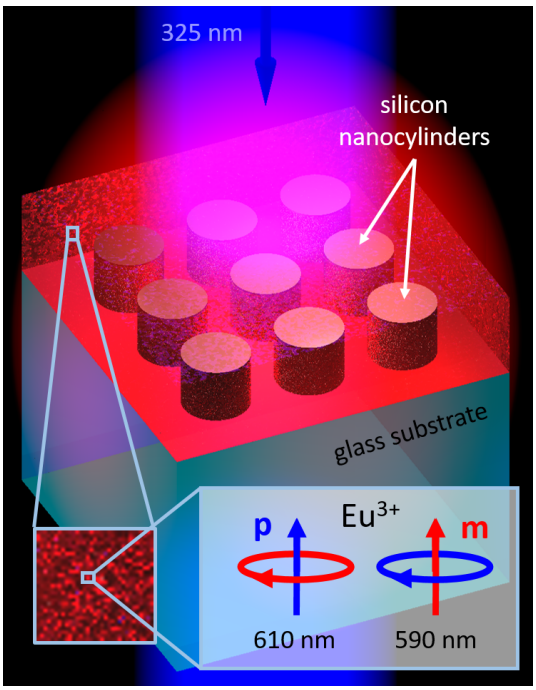

Figure 1: Artist's impression of Mie-resonant silicon nanocylinders covered by a thin layer of Eu^{3+} containing polymer.

Results and discussion

We fabricate two identical samples, each consisting of 20 nanocylinder metasurfaces with a footprint of 100 μm $\times$ 100 μm and nanocylinder radii varying between 96 nm and 146 nm (see Methods for details on the fabrication process). The lattice constant and cylinder height are fixed to 560 nm and 182 nm, respectively. A scanning-electron microscope (SEM) image of one of the fabricated metasurfaces is shown in Fig. 2 (a).

As a first step, the fabricated metasurfaces were characterized using near-normal incidence linear-optical transmittance spectroscopy.[26] A typical measured transmittance spectrum is shown in Fig. 2 (b) (yellow line). The spectrum exhibits several pronounced minima corresponding to Mie-type resonances of the silicon nanocylinders. Figure 2 (b) also shows a corresponding numerically calculated transmittance spectrum obtained via finite-element

calculations using the software package COMSOL Multiphysics (see Methods for details). In order to match the spectral position of the minima with those observed in the experiments, the height and radius of the cylinders are varied within the experimental accuracy limits, while the period is kept constant at its design value. Furthermore, we performed a multipole decomposition[27] of the modes excited in the silicon nanocylinders (see Supporting Information for the multipole decomposition results), revealing that the minimum at 920 nm in Fig. 2 (b) corresponds to the excitation of a magnetic dipole (MD) resonance, the minimum at 850 nm corresponds to an electric dipole (ED) resonance, and the minima at wavelengths below 700 nm originate from electric and magnetic quadrupole-dominated resonances. We measured the transmittance spectra for all 20 metasurfaces, each having different nanocylinder radius. As can be seen in Fig. 2 (c), in the transmittance spectra the Mie-resonances are red-shifting with increasing nanocylinder radius. The metasurfaces are sorted such that a larger array number corresponds to a larger radius. Corresponding calculated transmittance spectra are depicted in Fig. 2 (d). From our calculations, we can identify the effective nanocylinder height and radius for each of the metasurfaces by optimizing the agreement of the calculated transmittance spectrum with the respective experimental spectrum (see Supporting Information for the obtained metasurface geometrical parameters). We were able to precisely match the experimentally observed resonance positions, however, a discrepancy in the absolute transmittance levels remains, which we attribute to sample imperfections such as surface roughness. The difference between the nanocylinders sizes used in calculations and measured in a SEM is within a range of 20 nm. This small difference is likely due to the formation of a low-index layer at the surface of the nanocylinders, deviations of the silicon refractive index in the nanostructured sample as compared to the unstructured film used in ellipsometry measurements, and a slight tilt of the nanocylinder side walls.[28]

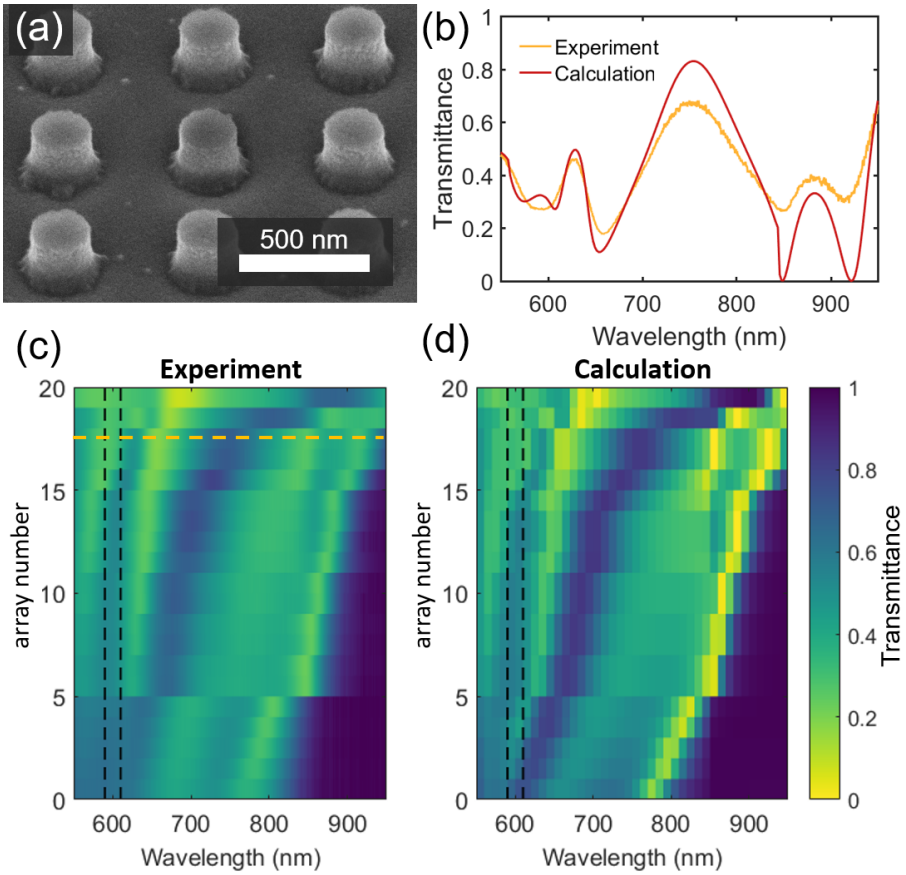

Figure 2: (a) Scanning electron micrograph of a typical silicon metasurface array before coating with the Eu^{3+} containing layer. (b) Experimentally measured and numerically calculated transmittance of a silicon metasurface with a nanocylinder radius of 131 nm. (c,d) Experimental and numerically calculated transmittance spectra for a series of silicon metasurfaces. The nanocylinder size increases with increasing array number. The dashed vertical lines indicate the wavelengths of the MD transition at 590 nm and ED transition at 610 nm of Eu^{3+}. The dashed horizontal line corresponds to the sample depicted in (b).

In Fig. 2 (c,d) the wavelengths of 590 nm and 610 nm, which correspond to the magnetic-dominated and electric dipole transitions of Eu^{3+}, respectively, are indicated as dashed lines. The spectral overlap of these transitions with the Mie-resonances varies for different nanocylinder radii. This allows us to study the influence of the Mie-modes of the nanocylinders on the enhancement of the different types of transitions in Eu^{3+}.

As a material incorporating luminescent Eu^{3+}, we used the alkylated europium complex (tris(α-henoyltrifluoroacetone)(1-octadecyl-2(-2-pyridyl)benzimidazole)europium(III)) abbreviated as $Eu(TTA)_3L18$. A schematic of the electronic energy-level structure of the Eu^{3+}

in this complex is shown in Fig. 3 (a). The material can be excited in the ultraviolet range and shows emission in the visible, which is associated with several radiative decay channels having the same upper energy level $^5D_0$, but several lower levels. A measured emission spectrum of Eu(TTA)$_3$L18 is shown in Fig. 3 (b). The Eu^{3+} emission line at $\lambda = 590\,\text{nm}$ is dominated by the magnetic dipole transition $^5D_0 \rightarrow ^7F_1$, while the strongest line in the emission spectrum at $\lambda = 610\,\text{nm}$ corresponds to the electric dipole transition $^5D_0 \rightarrow ^7F_2$.[29] Solutions of Eu(TTA)$_3$L18 complex and polystyrene in chloroform were mixed in the proportion 1:5 and spin coated on the metasurface array to produce a thin film with a thickness of approximately 200 nm, as measured in the unstructured areas of the sample.

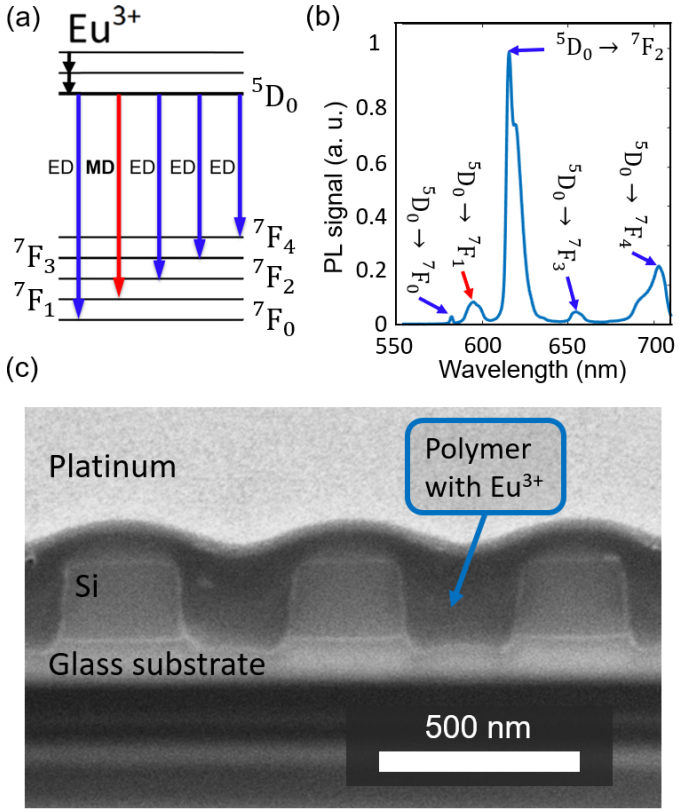

Figure 3: (a) Sketch of the energy-level structure of Eu^{3+}. (b) Measured emission spectra from the Eu^{3+} containing polymer layer coated onto a bare glass substrate. (c) SEM image of a focused ion-beam cross section of one of the metasurfaces after spin coating with the Eu^{3+} containing polymer.

A SEM image of a focused ion-beam cross section of one of the metasurfaces after applica-

tion of the Eu^{3+} containing polymer layer is displayed in Fig. 3 (c). Note that the application of the layer induces a slight red-shift of the resonances with respect to the spectra presented in Fig. 2 (c), which depends on the layer thickness. Furthermore, the layer leads to a modification of the multipolar composition of the metasurface response, adding a magnetic dipolar contribution to the previously strongly quadrupole-dominated resonances (see Supporting Information).

In order to investigate the fluorescence properties of the coated metasurface arrays, the Eu^{3+} was excited with a He-Cd laser, emitting at $\lambda = 325\,\mathrm{nm}$ wavelength. An 0.4NA objective was used to collect the emission from the sample. Interferometric narrow-band filters centered at 590 nm or 610 nm were placed in the recording channel in order to selectively detect the emission at the magnetic dipole or electric dipole transition, respectively. The emission was focused at the sensor of a Thorlabs 1500 M GE-TE CCD camera in order to record the fluorescence microscopy image. Further details on the measurement procedure including a sketch of the experimental setup are included in the Supporting Information. The results are summarized in Fig. 4. Fluorescence microscope images of a set of metasurfaces covered by a Eu^{3+} containing polymer layer, taken at the magnetic and electric dipole transition wavelengths, are shown in Fig. 4 (a,b), respectively. Both images were recorded using the same gain settings but different integration times of 4000 ms for the wavelength of 590 nm and 400 ms for the wavelength of 610 nm. This results in approximately equal intensities of the emission at 590 nm and 610 nm wavelength in the areas in between the metasurface arrays, i.e., the bare glass substrate covered by the Eu^{3+} containing polymer layer. Therefore, we can directly compare the enhancement values despite the different intrinsic emission strengths of the electric- and magnetic-dominated transition channels (see Fig. 3 (b)).

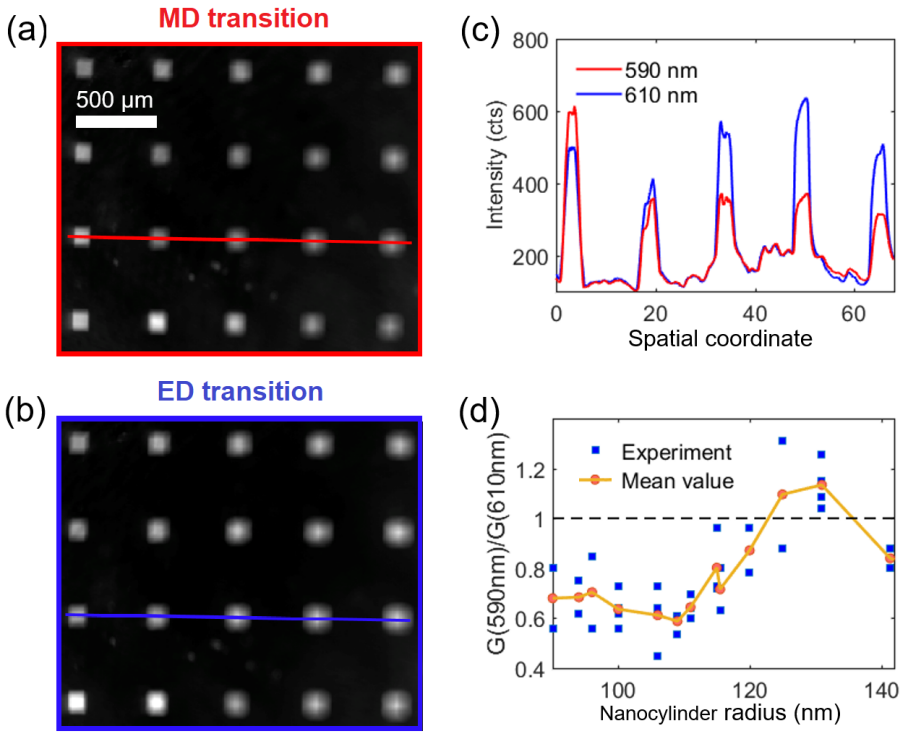

Figure 4: Fluorescence microscopy image of 20 metasurfaces (bright squares, each with a footprint of 100 μm $\times$ 100 μm) with different nanocylinder radii covered by a layer of Eu^{3+} containing polymer observed through narrow bandpass filters with a center wavelength of (a) 590 nm and (b) 610 nm. The images were taken at the same gain settings but different integration times of 4000 ms for the wavelength of 590 nm and 400 ms for the wavelength of 610 nm. (c) Emission intensity along the red and blue horizontal lines shown in (a,b). (d) Experimentally measured emission enhancement ratio G_{590}/G_{610} as a function of the nanocylinder radius.

Both images show the same set of 4×5 metasurfaces having different nanocylinder sizes. The metasurface regions appear brighter than the surrounding glass substrate regions at both wavelengths. We checked that from the uncoated metasurfaces no fluorescence signal was observed under these measurement conditions, so that the enhanced signal can be attributed to the Eu^{3+} emission. Importantly, the absolute enhancement is clearly different for different metasurfaces and different transitions. In order to quantify the differences in fluorescence enhancement in an exemplary fashion, Fig. 4 (c) illustrates the cross-sections along a horizontal cross section indicated by the red line in Fig. 4 (a) and the blue line in Fig. 4 (b). Each of the five peaks shown in Fig. 4 corresponds to a particular metasurface.

Clearly, metasurfaces with different nanocylinder sizes enhance the magnetic and electric dipole transitions with different efficiency. Most strikingly, the leftmost metasurface in the selected row shows a stronger enhancement for the magnetic-dominated dipole transition, while for all other metasurfaces in the row, the electric dipole transition is enhanced more strongly.

Next, we perform a systematic analysis of the experimentally measured enhancement values depending on the size of the silicon nanocylinders. The enhancement G_{590} (G_{610}) at the magnetic-dominated (electric) transition wavelength is defined as the ratio of the fluorescence intensity I_{590} (I_{610}) observed for the Eu^{3+} containing polymer layer covering a particular metasurface and the corresponding intensity observed for the same layer on the bare glass substrate next to the metasurface. Figure 4 (d) shows the emission enhancement ratio G_{590}/G_{610} as a function of the nanocylinder radius. Note that this quantity is closely related to the branching ratios of emission via the magnetic (electric) channel defined as $\beta_m = \frac{I_{590}}{I_{total}}$ ($\beta_e = \frac{I_{610}}{I_{total}}$), where I_{total} is the total collected fluorescence intensity. The solid blue squares correspond to the experimentally measured values of the emission enhancement ratio for individual metasurface arrays, the solid orange circles represent the mean value for several samples with the same nanocylinder radius. Note that we excluded measurement data from two of 40 individual samples, since they were overexposed according to the SEM images.

Clearly, the mean value of the emission enhancement ratio G_{590}/G_{610} shows a systematic dependence on the nanocylinder radius. The emission enhancement ratio is lower than 1 for the samples with nanocylinder radii below 120 nm, reaching a minimum of 0.6 for the sample with a nanocylinder radius of 109 nm. For larger radii, it then increases and reaches maximum of 1.12 for the sample with a radius of 131 nm. Finally, the emission enhancement ratio decreases again for the sample with even larger nanocylinder radius of 141 nm. This systematic dependence indicates that the enhancement stems from an emission enhancement due to coupling to the Mie-type resonances of the metasurfaces as they are shifted in and

out of spectral overlap with the electric and magnetic-dominated transitions of the Eu^{3+} via variation of the radius. Note, however, that there are two different reasons why the emission enhancement ratio G_{590}/G_{610} can deviate from the level of 1, which cannot be distinguished by our experiment alone. Specifically, the emission enhancement observed at 590 nm and 610 nm can differ due to the different nature of the emission from Eu^{3+} (electric or magnetic dipole) at the two wavelengths, but it could also be influenced by the difference in the emission wavelengths themselves, leading to a change in the spectral overlap with a particular Mie-resonance.

Thus, in order to clarify how the nature of the emission affects the enhancement, we perform numerical simulations to estimate the emission from the metasurfaces covered by a layer of low index polymer incorporating homogeneously distributed point dipole emitters with random orientation. Our method is based on the reciprocity principle.[26,30,31] The reciprocity principle can be formulated for a system consisting of two electric point dipoles: $\mathbf{p}_1 \cdot \mathbf{E}_2(\mathbf{r}_1) = \mathbf{p}_2 \cdot \mathbf{E}_1(\mathbf{r}_2)$, where $\mathbf{p}_1$ is the electric dipole moment of the first dipole placed at position $\mathbf{r}_1$ and producing an electric field $\mathbf{E}_1(\mathbf{r})$, and $\mathbf{p}_2$ is the electric dipole moment of the second dipole placed at position $\mathbf{r}_2$ and producing an electric field $\mathbf{E}_2(\mathbf{r})$. It is also possible to formulate the reciprocity principle for a system consisting of one magnetic and one electric point dipole: $\mathbf{m}_1 \cdot \mathbf{H}_2(\mathbf{r}_1) = \mathbf{p}_2 \cdot \mathbf{E}_1(\mathbf{r}_2)$, where $\mathbf{m}_1$ is the magnetic dipole moment of the first dipole placed at position $\mathbf{r}_1$ and producing an electric field $\mathbf{E}_1(\mathbf{r})$ and $\mathbf{p}_2$ is the electric dipole moment of the second dipole placed at position $\mathbf{r}_2$ and producing a magnetic field $\mathbf{H}_2(\mathbf{r})$. If we place the first dipole $\mathbf{p}_1$ ($\mathbf{m}_1$) on our sample and move the second dipole $\mathbf{p}_2$ far away along the direction (θ,ϕ), then the $\mathbf{E}_1(\mathbf{r}_2)$ represents the far field emitted by the first dipole coupled to the nanocylinder array in the direction (θ,ϕ) and $\mathbf{E}_2(\mathbf{r}_1)$ ($\mathbf{H}_2(\mathbf{r}_1)$) is the local electric (magnetic) field of the metasurface excited by a plane wave incident from the second dipole along the same direction (θ,ϕ). Thereby the reciprocity principle allows us to overcome the usual difficulties associated with the simulation of single dipole sources coupled to a periodic structure[32] and we are able to limit the computational domain

to an elementary cell with periodic boundary conditions. To compare our approach with a more established, yet computationally more demanding, method to calculate the emission properties of a periodic photonic nanostructure, we also performed calculations based on the inverse Floquet transformation.[32] The results are included as Supporting Information.

Figure 5 (a) shows a sketch of the elementary cell used in our calculations. The silicon cylinder (blue) is placed onto a glass substrate and covered by the Eu^{3+} containing polymer layer (green and red). The polymer was modeled with a refractive index of $n = 1.6$. Note that in the experiment, the excitation field from the 325 nm laser decays inside the active layer, such that the emitters in the upper part of the layer are more efficiently excited. To take this into account in our simulations, we divide the polymer layer into an active upper part (red) of thickness 180 nm and a passive lower part (green) of thickness 40 nm. Based on the experimentally measured transmittance of the 325 nm laser light through the polymer layer doped by Eu^{3+} ions, the thickness of the active layer of 180 nm is associated with a decay of the excitation illumination by a factor of 3. The elementary cell was excited by a plane wave incident from the upper half-space at polar angle θ and azimuthal angle ϕ. The emission enhancement via the magnetic transition G_{MD} can be estimated as:[33]

$$G_{\mathrm{MD}}(590\,\mathrm{nm}) = \frac{1}{P_{0,\mathrm{MD}}} \sum_{\theta,\phi,\mathrm{TE,TM}} \langle |\mathbf{H}(\mathbf{r};\theta,\phi)|^2 \rangle \sin\theta. \tag{1}$$

Here, $G_{\mathrm{MD}}(590\,\mathrm{nm})$ is the emission enhancement from the magnetic dipoles emitting at $\lambda = 590\,\mathrm{nm}$, which are assumed to be randomly oriented and homogeneously distributed inside the active upper part of the polymer layer (red region in Fig. 5 (a)). $\mathbf{H}(\mathbf{r};\theta,\phi)$ is the local magnetic field excited by either TE or TM polarized plane wave with a wavelength of 590 nm incident from the upper half-space at polar angle θ and azimuthal angle ϕ. To better match the experimental conditions, only emission under solid angles corresponding to the 0.4NA objective are considered in the summation. $\langle ... \rangle$ denotes the spatial averaging over the active part of the polymer layer. Similar to the experiment, the calculated emission en-

hanced by the nanocylinders array is divided by the magnetic dipole emission $P_{0,\mathrm{MD}}$ collected by 0.4NA objective for the case of a bare glass substrate covered by a Eu^{3+} containing polymer layer of a thickness of 180 nm (measured by electron microscopy of a focused-ion-beam cross section through the unstructured area of the sample) and calculated using the same approach. Further details on the numerical calculations are included in the Methods section. Note that our approach to calculate the numerical emission enhancement ratio as a function of the nanocylinder diameter takes both expected changes of the radiative decay rate and of the collection efficiency into account, and is thus directly related to the corresponding fluorescence enhancement observed in experiment. However, it neglects the complex electronic level structure of the Eu^{3+}, the finite quantum efficiencies of the transitions, the details of the excitation regime present in experiment and a possible excitation enhancement. Therefore, it does not allow for a quantitative prediction of the absolute fluorescence enhancement.

Equivalently, for the case of electric dipole emission, we obtain:

$$G_{\mathrm{ED}}(610\,\mathrm{nm}) = \frac{1}{P_{0,\mathrm{ED}}} \sum_{\theta,\phi,\mathrm{TE,TM}} \langle |\mathbf{E}(\mathbf{r};\theta,\phi)|^2 \rangle \sin\theta. \tag{2}$$

Here, $G_{\mathrm{ED}}(610\,\mathrm{nm})$ is the emission enhancement from the electric dipoles emitting at $\lambda = 610\,\mathrm{nm}$, which are also assumed to be randomly oriented and homogeneously distributed inside the active part of the polymer layer. $\mathbf{E}(\mathbf{r};\theta,\phi)$ is the local electric field excited by either TE or TM polarized plane wave with wavelength of 610 nm incident from the upper half-space at polar angle θ and azimuthal angle ϕ. $P_{0,\mathrm{ED}}$ is the electric dipole emission for the case of bare glass substrate covered by a polymer layer of thickness 180 nm. The collection NA and referencing procedure are the same as for the calculation performed in the case of the magnetic dipole.

We sum over both TE and TM polarizations and the directions of the incident plane wave, while the polar angle of incidence θ takes values in the range of $[0°, 45°]$, corresponding to the 0.4NA of the collection objective. The azimuthal angle ϕ that takes values within the

range of $[0°, 45°]$ corresponding to the symmetry of the two-dimensional square lattice.

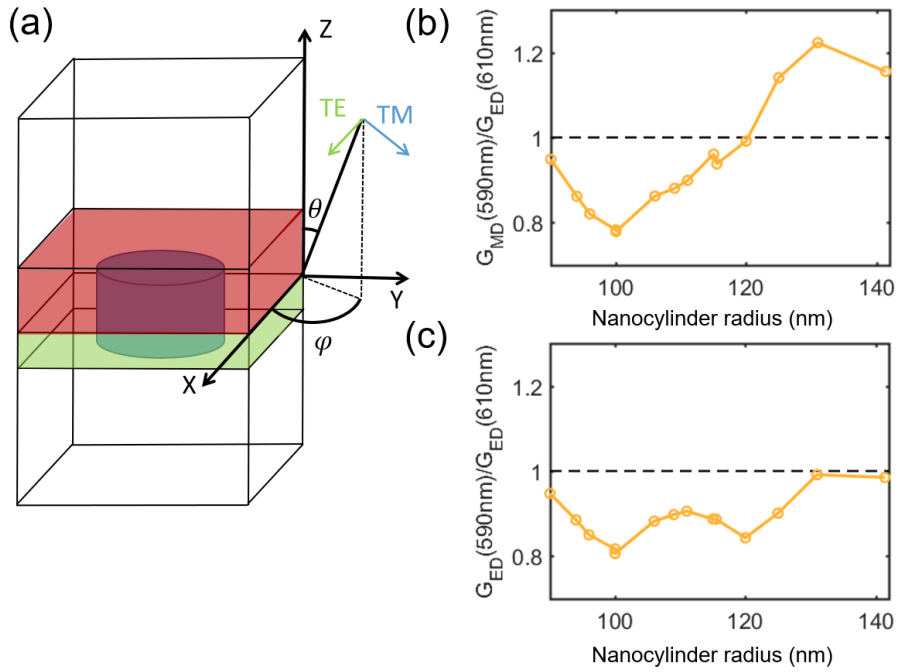

Figure 5: Numerical simulations of the emission enhancement for electric and magnetic dipoles: (a) Sketch of the computational domain. The red and green layer, indicates the emitting and the inactive Eu^{3+}-containing polymer layers in our simulations. (b) Calculated ratio of the *magnetic* dipole emission enhancement at 590 nm wavelength and the electric dipole emission enhancement at 610 nm wavelength as a function of nanocylinder radius. (c) Calculated ratio of the *electric* dipole emission enhancement at 590 nm wavelength and the electric dipole emission enhancement at 610 nm wavelength.

Figure 5 (b) shows the calculated emission enhancement ratio $G_{MD}(590\,\text{nm})/G_{ED}(610\,\text{nm})$ as a function of the nanocylinder radius. In our calculations, we used the geometrical parameters of the nanocylinders that provided the best fit for the transmittance spectra of corresponding sample (see Fig. 2). As one can note, we obtain a good qualitative agreement with the experimental data (compare Fig. 4 (d) and Fig. 5 (b)). Indeed, all the major trends observed in the experimental emission enhancement ratio dependence on the nanocylinder diameter are well reproduced, with only moderate discrepancies in the values.

Note, however, that the absolute values for the emission enhancement appear approximately four times higher in the experiment, independent of the nanocylinder radius. This may be due to several reasons. Firstly, the calculations do not consider the level structure

of the Eu^{3+}, while the fact that the transitions at wavelengths of 590 nm and 610 nm, as well as several other transition lines originate from the same upper level leads to additional competitive enhancement and depletion mechanisms.[1] Secondly, a possible excitation enhancement by the nanocylinder arrays can increase the fluorescence signal in experiments. The proper implementation of excitation enhancement in calculations is not possible due to the lack of the dispersion data in UV for the material of the nanocylinders and due to the complex illumination configuration. Thirdly, sample imperfections affect the near field and cause additional scattering, which can potentially enhance the outcoupling and collection efficiency in the experiment. In particular, the upper surface of the Eu^{3+} containing layer is assumed as flat in the numerical model, while it shows a wavy structure in experiment (compare Fig. 3 (c)). Finally, the orientation or distribution of the Eu^{3+} ions within the polymer layer may be inhomogeneous.

As a final step, we also calculated the emission enhancement ratio $G_{\mathrm{ED}}(590\,\mathrm{nm})/G_{\mathrm{ED}}(610\,\mathrm{nm})$ at a wavelength of 590 nm assuming that the emission originates purely from electric dipole transition by replacing the magnetic field in Eq. 1 by the electric field. This result is shown in Fig. 5 (c). One can note that the behavior of the experimental data in Fig. 4 (d) is qualitatively different compared to the calculations assuming electric dipole emission at 590 nm wavelength. This result underpins that the fluorescence maximum at 590 nm in the Eu^{3+} spectrum remains magnetic-dipole dominated also in the presence of the metasurface. Based on our numerical simulations, we can conclude that the change of the emission enhancement ratio as a function of nanocylinder diameter will be mainly due to the different dipolar nature of the two transitions, while the mere difference in emission wavelength plays a minor role.

In conclusion, we have experimentally demonstrated the enhancement of spontaneous emission of Eu^{3+} ions by dielectric metasurfaces composed of Mie-resonant silicon nanocylinders. By fabricating metasurfaces featuring different nanocylinder radii, we have swept the position of Mie resonances having a strong quadrupolar contribution over the spectral range of the electric and magnetic-dominated dipole transitions of the Eu^{3+}. We have observed

a systematic change of the branching ratio of emission via the two different channels. Especially, we have experimentally shown, for the first time, that Mie-resonant all-dielectric metasurfaces allow for selective enhancement of the magnetic dipole emission over the electric dipole emission for a proper choice of the metasurface geometry. We have confirmed our observations with numerical simulations. Our results on the manipulation of magnetic dipole emission by designed resonant photonic nanostructures open many new pathways for future research on magnetic light-matter interactions in the research fields of active dielectric nanophotonics, light-emitting metasurfaces and nanoantennas, as well as chiral and nonlinear nano-optics, to name just a few.

Methods

Sample fabrication. For fabrication of silicon disks on the glass substrate we first deposit thin-films of hydrogenated amorphous silicon (a-Si:H) with a thickness of 182 nm, using plasma-enhanced chemical vapour deposition (PECVD) at a temperature of 250° C on standard microscope cover slips. Next, the substrates are spin-coated with the negative-tone electron-beam resist maN-2403. The nanocylinders are then defined by electron-beam lithography (EBL) in combination with inductively coupled plasma (ICP) etching of the silicon thin-film, where the exposed electron-beam resist is used as an etch mask. As etch gases, we used SF_6 (1.8 sccm) and CHF_3 (50 sccm). Etching was performed at 20° C with 10 mTorr at 500 W induction power and 15 W bias power. Finally, residual resist and organic solvent residue left on the sample were removed using oxygen plasma. To render the sample conductive for imaging with an electron microscope, we cover it with a thin (15 nm) transparent layer of indium tin oxide (ITO) using sputter coating at 1.5 mTorr pressure, 20 sccm Argon flow, 60 W Power, and 8×10^{-7} Torr base pressure.

Transmittance simulations. An elementary unit cell with Floquet periodic boundary conditions and two ports, one at the top and one at the bottom, was used. The top port

acted as a source exciting a normally incident plane wave. The reflected, transmitted and diffracted light was detected by both ports. The glass substrate was modeled with a refractive index of $n = 1.51$. For the optical material parameters of the a-Si:H, we used experimental data obtained from ellipsometry measurements on unstructured a-Si:H films.

Acknowledgement

Financial support by the Thuringian State Government within its ProExcellence initiative (ACP^{2020}) and the German Research Foundation (STA 1426/2-1) is gratefully acknowledged. K.E.C., D.N.N. and Y.S.K. acknowledge the support by the Australian Research Council (DP150103733). Y.S.K. acknowledges a support from the Humboldt Foundation. S.N. acknowledges financial support by the Karlsruhe School of Optics and Photonics and by the DFG Priority Programm 1839 Tailored Disorder. The authors also acknowledge their participation in the Erasmus Mundus NANOPHI project, contract number 2013 5659/002-001. This work was performed in part at the ACT node of the Australian National Fabrication Facility, a company established under the National Collaborative Research Infrastructure Strategy to provide nano- and microfabrication facilities for Australia's researchers. We are grateful to the company JCMwave for their free provision of the FEM Maxwell solver JCMsuite, with which the Floquet simulations in this work have been performed. We acknowledge fruitful discussions with M. Decker.

Supporting Information Available

The Supporting Information is available free of charge on the ACS Publications website at DOI (to be filled): Table of the metasurface geometrical parameters used in numerical calculations. Description of the experimental setup. Multipole analysis of the modes excited in nanocylinders. Inverse Floquet transformation for far-field emission calculations. This material is available free of charge via the Internet at `http://pubs.acs.org/`.

References

(1) Taminiau, T. H.; Karaveli, S.; van Hulst, N. F.; Zia, R. Quantifying the magnetic nature of light emission. Nat. Commun. **2012**, 3, 979.

(2) Kasperczyk, M.; Person, S.; Ananias, D.; Carlos, L.D; Novotny, L. Excitation of magnetic dipole transiitons at optical frequencies. Phys. Rev. Lett. **2015**, 114, 163903.

(3) Brewer, N.R.; Buckholtz, Z.N.; Simmons, Z.J.; Mueller, E.A.; Yavuz, D.D. Coherent magnetic response at optical frequencies using atomic transitions. Phys. Rev. X **2017**, 7, 011005.

(4) Purcell, E. M. Spontaneous emission probabilities at radio frequencies. Phys. Rev. **1946**, 69, 681.

(5) Baranov, D.G.; Savelev, R.S.; Li, S.V.; Krasnok, A.E.; Alú, A. Modifying magnetic dipole spontaneous emission with nanophotonic structures. Laser Photonics Rev. **2017**, 11, 1600268.

(6) Noginova, N.; Zhu, G.; Mayy, M.; Noginov, M.A. Magnetic dipole based systems for probing optical magnetism. J. Appl. Phys. **2008**, 103, 07E901.

(7) Karaveli, S.; Zia, R. Spectral Tuning by Selective Enhancement of Electric and Magnetic Dipole Emission. Phys. Rev. Lett. **2011**, 106, 193004.

(8) Ni, X.; Naik, G.V.; Kildishev, A.V.; Barnakov, Y.; Boltasseva, A.; Shalaev, V.M. Effect of metallic and hyperbolic metamaterial surfaces on electric and magnetic dipole emission transitions. Appl. Phys. B **2011**, 103, 553.

(9) Hussain, R.; Keene, D.; Noginova, N.; Durach, M. Spontaneous emission of electric and magnetic dipoles in the vicinity of thin and thick metal. Opt. Express **2014**, 22, 7744.

(10) Aigouy, L.; Cazé, A.; Gredin, P.; Mortier, M.; Carminati, R. Mapping and Quantifying Electric and Magnetic Dipole Luminescence at the Nanoscale. Phys. Rev. Lett. **2014**, 113, 076101.

(11) Hussain, R.; Kruk, S.S.; Bonner, C.E.; Noginov, M.A.; Staude, I.; Kivshar, Y.S.; Noginova, N.; Neshev, D.N. Enhancing Eu^{3+} magnetic dipole emission by resonant plasmonic nanostructures. Opt. Lett. **2015**, 40, 1659.

(12) Choi, B.; Iwanaga, M.; Sugimoto, Y.; Sakoda, K.; Miyazaki, H. T. Selective Plasmonic Enhancement of Electric- and Magnetic-Dipole Radiations of Er Ions. Nano Lett. **2016**, 16, 5191-5196.

(13) Murai, S.; Saito, M.; Sakamoto, H.; Yamamoto, M.; Kamakura, R.; Nakanishi, T.; Fujita, K.; Verschuuren, M. A.; Hasegawa, Y.; Tanaka, K. Directional outcoupling of photoluminescence from Eu(III)-complex thin films by plasmonic array. APL Photon. **2017**, 2, 026104.

(14) Kuznetsov, A.I.; Miroshnichenko, A.E.; Brongersma, M.L.; Kivshar, Y.S.; Lukyanchuk, B. Optically resonant dielectric nanostructures. Science **2016**, 354.

(15) Decker, M.; Staude, I. Resonant dielectric nanostructures: A low-loss platform for functional nanophotonics. J. Opt. **2016**, 18, 103001.

(16) Jahani, J.; Jacob, Z. All-dielectric metamaterials. Nat. Nanotech. **2016** 11, 23.

(17) Staude, I.; Schilling, J. Metamaterial-inspired silicon nanophotonics. Nat. Photonics **2017**, 11, 274.

(18) Kruk, S.; Kivshar, Y.S. Functional meta-optics and nanophotonics governed by Mie resonances. ACS Photonics **2017**, 4(11), 2638-2649.

(19) Neshev, D.N.; Aharonovich, I. Optical metasurfaces: new generation building blocks for multi-functional optics. Light Sci. & Appl. **2018**, 7, 2047.

(20) Rolly, B.; Bebey, B.; Bidault, S.; Stout, B.; Bonod, N. Promoting magnetic dipolar transition in trivalent lanthanide ions with lossless Mie resonances. Phys. Rev. B **2012**, 85, 245432.

(21) Schmidt, M.K.; Esteban, R.; Sáenz, J.J.; Suárez-Lacalle, I.; Mackowski, S.; Aizpurua, J. Dielectric antennas - a suitable platform for controlling magnetic dipolar emission. Opt. Exp. **2012**, 20, 13636.

(22) Zambrana-Puyalto, X.; Bonod, N. Purcell factor of spherical Mie resonators. Phys. Rev. B **2015**, 91, 195422.

(23) Feng, T.; Xu, Y.; Liang, Z.; Zhang, W. All-dielectric hollow nanodisk for tailoring magnetic dipole emission. Opt. Lett. **2016**, 41, 5011.

(24) Li, J.; Verellen, N.; Van Dorpe, P. Enhancing Magnetic Dipole Emission by a Nano-Doughnut-Shaped Silicon Disk. ACS Photonics **2017**, 4(8), 1893-1898.

(25) Sanz-Paz, M.; Ernandes, C.; Esparza, J.U.; Burr, G.W.; van Hulst, N.F.; Maitre, A.; Aigouy, L.; Gacoin, T.; Bonod, N.; Garcia-Parajo, M.F.; Bidault, S.; Mivelle, M. Enhancing Magnetic Light Emission with All-Dielectric Optical Nanoantennas. Nano Lett. **2018**, 18(6), 3481-3487.

(26) Vaskin, A.; Bohn, J.; Chong, K.E.; Bucher, T.; Zilk, M.; Choi, D.-Y.; Neshev, D.N.; Kivshar, Y. S.; Pertsch, T.; Staude, I. Directional and Spectral Shaping of Light Emission with Mie-Resonant Silicon Nanoantenna Arrays. ACS Photonics **2018**, 5(4), 1359-1364.

(27) Grahn, P.; Shevchenko, A.; Kaivola, M. Electromagnetic multipole theory for optical nanomaterials. New J. Phys. **2012**, 14, 09303.

(28) Arslan, D.; Chong, K. E.; Miroshnichenko, A. E.; Choi, D.-Y.; Neshev, D. N.; Pertsch,

T.; Kivshar Y. S.; Staude, I. Angle-selective all-dielectric Huygens' metasurfaces. J. Phys. D: Appl. Phys. **2017**, 50, 434002.

(29) Tsaryuk, V.I.; Zhuravlev, K.P.; Zolin, V.F.; Kudryashova, V.A.; Legendziewicz, J.; Szostak, R. Luminescence efficiency of aromatic carboxylates of europium and terbium. J. Appl. Spectrosc. **2007**, 74, 51.

(30) Landau, L.D.; Lifshits, E.M.; Pitaevskii, L. Electrodynamics of continuous media. Pergamon press Oxford **1984**, 8.

(31) Kahl M.; Voges, E. Analysis of plasmon resonance and surface-enhanced Raman scattering on periodic silver structures. Phys. Rev. B **2000**, 61, 14078.

(32) Burger, S.; Zschiedrich, L.; Greiner, H.J.; Schmidt, F. Numerical analysis of nanostructures for enhanced light extraction from OLEDs. Proc. SPIE, **2013**, 8641.

(33) Zhang S.; Martins, E. R.; Diyaf A. G.; Wilson, J. I. B.; Turnbull, G. A.; Samuel, I. D. W. Calculation of the emission power distribution of microstructured OLEDs using the reciprocity theorem. Synth. Met. **2015**, 205, 127.

Manipulation of electric and magnetic dipole emission from Eu^{3+} with Mie-resonant metasurfaces: Supporting Information

Aleksandr Vaskin,[*,†] Soheila Mashhadi,[‡] Michael Steinert,[†] Katie E. Chong,[¶] David Keene,[§] Stefan Nanz,[∥] Aimi Abass,[⊥] Evgenia Rusak,[∥,¶] Duk-Yong Choi,[#] Ivan Fernandez-Corbaton,[⊥] Thomas Pertsch,[†] Carsten Rockstuhl,[⊥,∥] Mikhail A. Noginov,[‡] Yuri S. Kivshar,[¶] Dragomir N. Neshev,[¶] Natalia Noginova,[‡] and Isabelle Staude[†]

†*Institute of Applied Physics, Abbe Center of Photonics, Friedrich Schiller University Jena, 07745 Jena, Germany*

‡*Center for Materials Research, Norfolk State University, Norfolk, VA 23504*

¶*Nonlinear Physics Centre, Australian National University, Canberra ACT 2601, Australia*

§*Center for Materials Research, Norfolk State University, Norfolk, VA 23504*

∥*Institute of Theoretical Solid State Physics, Karlsruhe Institute of Technology, 76131 Karlsruhe, Germany*

⊥*Institute of Nanotechnology, Karlsruhe Institute of Technology, 76021 Karlsruhe, Germany*

#*Laser Physics Centre, Research School of Physics and Engineering, The Australian National University, Canberra, ACT 2601, Australia*

E-mail: aleksandr.vaskin@uni-jena.de

Number of pages: 9

Number of figures: 5

Metasurface geometrical parameters used in numerical calculations.

array number	radius (nm)	height (nm)
1	90	150
2	94	150
3	96	150
4	100	150
5	100	155
6	106	160
7	106	160
8	109	160
9	109	160
10	111	161
11	111	161
12	115	165
13	115	165
14	115.5	160.6
15	120	160
16	125	165
17	131	165
18	131	165
19	141.4	171.7
20	160	170

Experimental fluorescence microscopy setup

A sketch of the setup used in fluorescence microscopy measurements is depicted in Fig. S1. The sample was covered by a Eu^{3+} containing polymer. The Eu^{3+} was excited by a HeCd

laser with a wavelength of 325 nm and intensity of 20 mW/cm^2. The fluorescence from the sample was collected by a 0.4 NA objective, propagated through a bandpass filter (center wavelength of 590 nm and 610 nm, respectively, bandwidth 10 nm), and imaged at the CCD camera sensor by the camera objective lens.

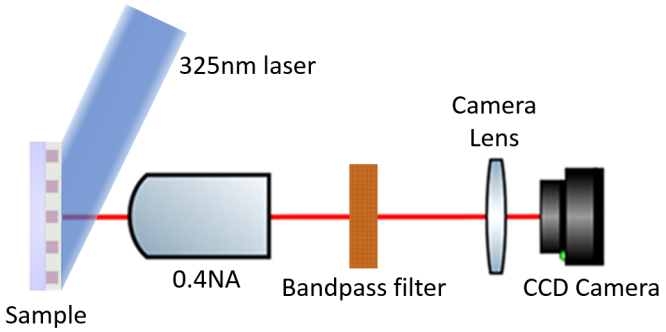

Figure S1: Sketch of the experimental setup used for fluorescence microscopy.

Multipole decomposition

In order to identify the multipolar order of the resonances that can be observed in the transmittance spectra of the silicon nanocylinder metasurfaces, we performed a multipole decomposition using the commercially available software package Comsol Multiphysics and the method described in Grahn *et al.*[1] We chose the metasurface with a nanocylinder radius of 131 nm and a height of 165 nm as exemplary case, and excite it by a normally incident plane wave. We then decompose the field inside the nanocylinder into the Mie-modes. The results are shown in Fig. S2 (a). Note that in the 590 nm to 610 nm range the metasurface response is dominated by the electric quadrupole mode. For comparison, Fig. S2 (b) shows the experimental and calculated transmittance spectra for the same metasurface. Also, Fig. S3 shows the electric and magnetic field distribution for a vertical cut through the center of the nanocylinder at the wavelengths of the magnetic (590 nm) and electric (610 nm) dipole transitions of Eu^{3+}.

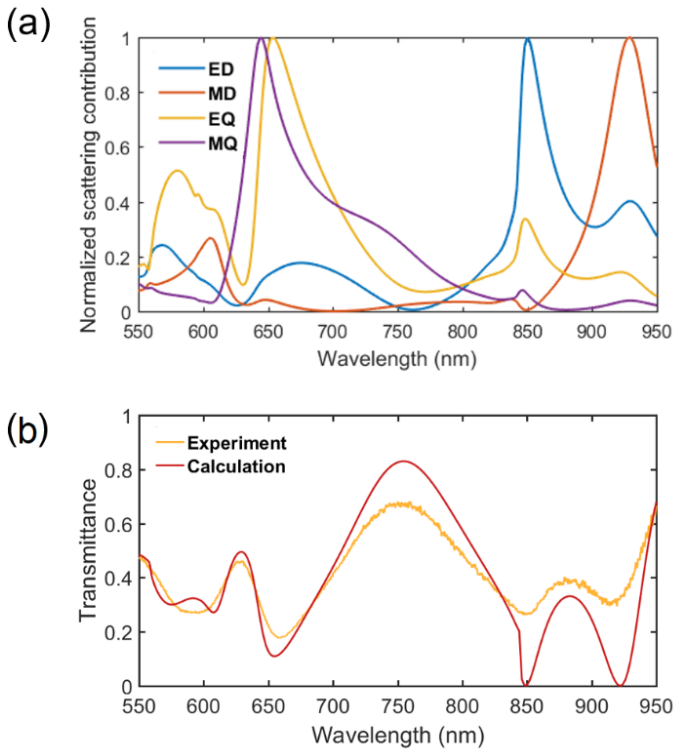

Figure S2: (a) Multipole decomposition of the fields excited in a nanocylinder by a normally incident plane wave for a sample with nanocylinder radius of 131 nm and height of 165 nm. ED, MD, EQ, and MQ denote the electric dipole, magnetic dipole, electric quadrupole, and magnetic quadrupole contributions, respectively. (b) Corresponding experimental and calculated transmittance spectra.

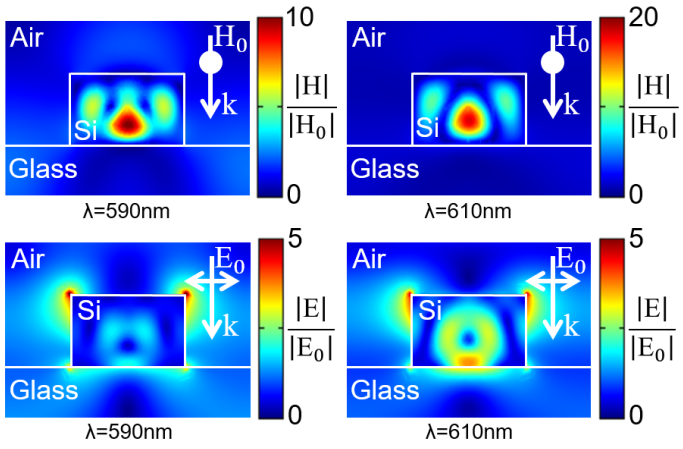

Figure S3: Electric and magnetic field distributions shown at a vertical cut plane through the center of the nanocylinder, for plane wave excitation at normal incidence. The nanocylinder radius is 131 nm and its height is 165 nm.

Figure S4 shows the multipole decomposition for case that the metasurface is covered by the Eu^{3+} containing polymer layer. Note that all features are red-shifted and that in the 590 nm to 610 nm range the metasurface response is dominated by magnetic dipole, electric quadrupole, and magnetic quadruple contributions.

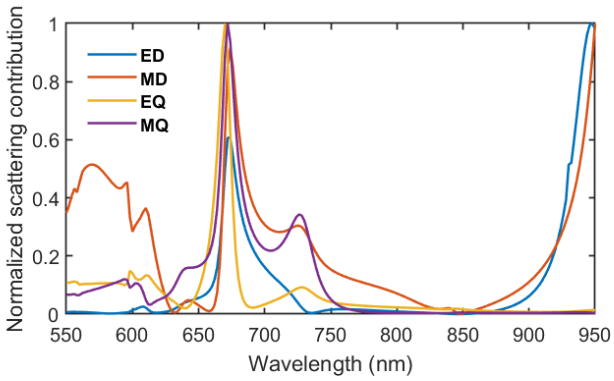

Figure S4: Multipole decomposition of the fields in a nanocylinder covered by the Eu^{3+} containing polymer layer (see Fig. 5(a)) excited by a normally incident plane wave for a sample with nanocylinder radius of 131 nm and height of 165 nm. ED, MD, EQ, and MQ denote the electric dipole, magnetic dipole, electric quadrupole, and magnetic quadrupole contributions, respectively.

Inverse Floquet transformation for far-field emission calculations

In order to deduce the far field and the dipole emission enhancement in a more direct way, without utilizing the reciprocity principle, while still keeping the computational effort feasible, we made use of a supercell method that employs an inverse Floquet transformation.[2] This algorithm allows to reconstruct the emission response of an isolated dipole in a periodic system by combining the response of periodically arranged dipoles with varying phase relations along the periodic boundaries.

Rigorous simulations of the unit cell were done using the FEM solver JCMsuite.[3] This software does neither allow a direct simulation of magnetic dipoles, nor does it provide the magnetic field of an electric dipole. We therefore exploited the duality of Maxwell's equations: We simulated an electric dipole, but having the material parameters permittivity and permeability transformed under the duality transformation[4] $\epsilon \to \mu$ and $\mu \to \epsilon$. The

electric field $\mathbf{E}_d$ of an electric dipole with such material parameters is then proportional to the magnetic field of a magnetic dipole with regular material parameters: $\mathbf{E}_d = -c\mathbf{B}$, where c is the speed of light. To retrieve the electric field of the magnetic dipole, we applied in a last step the Maxwell-Ampere equation in Fourier space, $i\mathbf{k} \times \mathbf{B} = -i\mu_0\epsilon_0\omega\mathbf{E}$. The necessary plane wave decomposition of the far field was calculated using a post process in JCMsuite.

The emission occurring in the polymer layer is modeled as a superposition of different dipole emitters. To achieve a sufficiently fine resolution of the dipole response inside the unit cell, we simulated four laterally different dipole positions: In the center of the unit cell, close to the corner of the unit cell, close to the edge of the unit cell on the symmetry plane, and on the diagonal at the half distance between the center and the corner. For the positions at the corner and the edge, we slightly displaced the dipole from the high symmetry points by 5 nm towards the interior of the unit cell to avoid edge effects in the FEM simulation. The z-position of the dipoles was kept constant at a distance of 20 nm above the silicon disk, which corresponds to the center plane of the polymer layer. We simulated at each position and at both wavelengths, 590 nm and 610 nm, for the polarizations in x-, y-, and z-direction and for electric and dual magnetic dipole.

In each simulation of a unit cell, dipoles with the same periodicity like the nanodisks were simulated with a certain phase relation between them that was determined by the number of supercells. To recover the field of an isolated dipole in the periodic system, an inverse Floquet transformation was performed, in which the solutions for the different phase relations where superposed. We used 64 supercells in the simulation, which provided enough accuracy while still being computationally feasible.

We also performed a simulation of the unit cell without the silicon nanodisk, but keeping the z-position of the dipoles the same. The emission result of this simulation was used to normalize the emission in the presence of the nanoantennas. This normalization was done in two ways: First, we averaged the emission of the magnetic and electric dipole emitters over the three polarizations and normalized the dipole emission at each position individually by

the result of the flat reference simulation. As a second calculation, we averaged the emission results also over the positions and normalized the final value.

The results of the simulations is shown in Fig. S5 (a). For comparison, we also depict the far-field emission distribution calculated for the same system using reciprocity principle in Fig. S5 (b). In these simulations, to emulate a point dipole we evaluate the fields Eq. 2 at the point located at 20 nm above the center of the nanocylinder. As one can note, the results obtained by the two very different approaches are in excellent agreement.

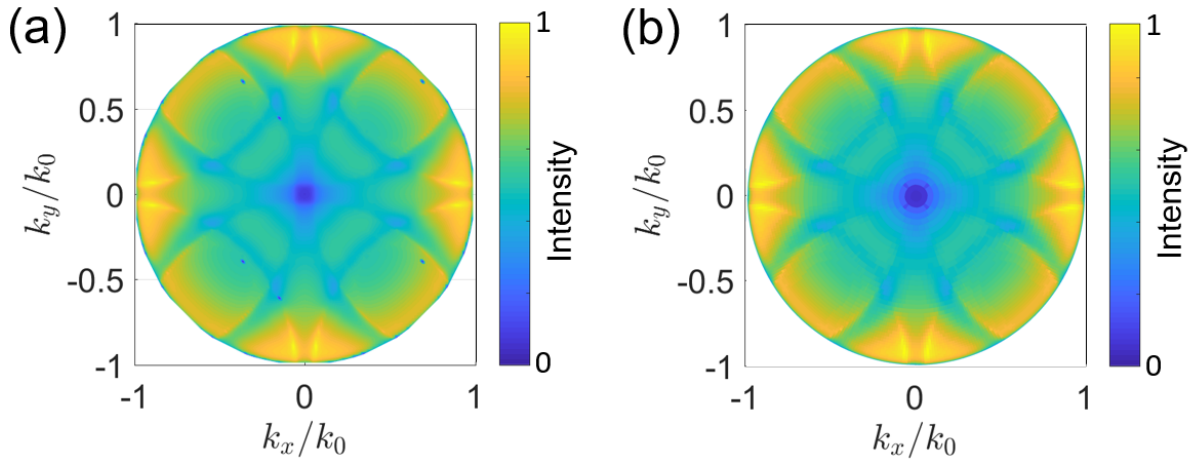

Figure S5: (a) Calculated angular emission distribution using on inverse Floquet transform. (b) Calculated angular emission distribution calculated using the reciprocity principle. Both cases simulate a point magnetic dipole emitting at 590 nm and located 20 nm above the center of the nanocylinder.

References

(1) P. Grahn, A. Shevchenko, and M. Kaivola, Electromagnetic multipole theory for optical nanomaterials, New Journal of Physics 14, 093033 (2012).

(2) S. Burger, L. Zschiedrich, H. J. Greiner and F. Schmidt. Numerical analysis of nanostructures for enhanced light extraction from OLEDs. Proc. SPIE, 8641:86410B, 2013.

(3) J. Pomplun, S. Burger, L. Zschiedrich, and F. Schmidt, Adaptive finite element method for simulation of optical nano structures. Phys. Stat. Sol. 244, 3419-3434, 2007.

(4) I. Fernandez-Corbaton and G. Molina-Terriza. Role of duality symmetry in transformation optics. Phys. Rev. B, 88, 085111, 2013.